Global ballooning instabilities in a Heliotron J plasma

Osamu Yamagishi,[a] Yuji Nakamura, and Katsumi Kondo
Graduate School of Energy Science, Kyoto University, Gokasho, Uji, Kyoto 611-0011, Japan

Noriyoshi Nakajima
National Institute for Fusion Science, Toki 509-5292, Japan

(Received 18 February 2002; accepted 17 April 2002)

The global ballooning stability in a Heliotron J plasma [M. Wakatani *et al.*, Nucl. Fusion **40**, 569 (2000)] is studied by use of the CAS3D code (code for analysis of stability in three-dimensional systems) [C. Schwab, Phys. Fluids **5**, 3195 (1993)]. The global mode has strong toroidal mode coupling so that the mode structure is typically a helical type. The mode structure of the pressure driven modes, including the interchange mode, is discussed. The comparison between the local and global modes is also shown. The eigenvalue as well as eigenfunction shows good agreement. © *2002 American Institute of Physics.* [DOI: 10.1063/1.1485074]

I. INTRODUCTION

Global stability of ideal ballooning modes in Heliotron J[1,2] is investigated by use of the CAS3D stability code.[3,4] An equilibrium configuration used in this study is Mercier stable, but a previous study of local stability showed that the local ballooning modes can be unstable.[5] The local modes in Heliotron J plasma have strong α dependence. Here, α is a label of the field line on a flux surface. This indicates the strong toroidal mode coupling of the global mode,[6,7] which is distinct from the ballooning mode in a tokamak localized only poloidally. The toroidal mode coupling can cause the global modes in the helical systems to be localized on the flux of specific field lines, and such modes have been found in Refs. 8 and 9 in the large helical device (LHD) equilibria. In these papers, it has been found that the mode structure can be categorized by the toroidal mode number n of the perturbation. In the Mercier unstable equilibria, the mode changes as n varies: low-n ($n<M$) yields the interchange mode, moderate-n ($n\sim M$) the interchange or tokamak-like ballooning mode, and high-n ($n\gg M$) the helical ballooning mode. In the Mercier stable equilibria, on the other hand, there exist only helical ballooning modes with toroidal mode number $n\gtrsim M$, and the $n<M$ mode is stable. Here, M is the number of toroidal field periods.

The toroidal mode coupling of the global modes occurs through the equilibrium M number. Previously, we had expected that the global mode in Heliotron J would be stable for very low toroidal mode number $n<M$, but the critical toroidal mode number for the instability is not so high; $n\sim 10$, because in the case of the $M=4$ Heliotron J, M is not as large as the $M=10$ LHD. It will be shown that even the $n\sim 10$ mode can become unstable and the mode structure is typically a helical type with strong toroidal mode coupling. This is consistent with the global results in the Mercier stable LHD equilibrium.[9] We will discuss the properties of the helical ballooning mode in the Mercier stable Heliotron J plasma, and why the non-low n number is required for the instability in the Mercier stable equilibria.

In Sec. II, the results of global stability are shown. In Sec. III and IV, the properties of the mode structure in Heliotron J plasma and how mode coupling occurs are discussed. The role of equilibrium quantities, in particular the local shear and the curvature of the field line, is discussed in Sec. V. The global modes are compared with local modes in Sec. VI. Conclusions are given in Sec. VII.

II. GLOBAL MODES IN A HELIOTRON J PLASMA

The local ballooning stability was previously investigated in a standard configuration of Heliotron J plasma.[5] The equilibrium was prescribed to be Mercier stable without flowing net current. The local ballooning instabilities were found in spite of the good Mercier stability. We investigate the stability of the global modes in the same configuration. For the global analysis, we use the CAS3D stability code.[3] The magnetohydrodynamic (MHD) equilibrium that is needed for the input of CAS3D is calculated by the VMEC code.[10] The pressure profile is almost prescribed as being broad; $p=p(0)(1-\hat{\chi}^2)^2$, unless otherwise remarked. Here, $\hat{\chi}$ is a normalized poloidal flux. The version of CAS3D code is CAS3D2, and this can calculate the MHD spectra assuming the incompressibility. We consider fixed boundary modes only, although the code can treat free boundary modes.

The mode number of the perturbation is given as an input for the CAS3D code. Normally the mode is destabilized by the destabilizing energy around a rational surface corresponding to its mode number; $\iota=n/m$, and so is called the resonant mode. However, if we consider only the resonant modes, the important effect due to the mode coupling on the stability is possibly ignored. The method for mode selection in this study is represented in the Appendix. The CAS3D2 code treats the perpendicular perturbed vector $\boldsymbol{\xi}_\perp$. Thus, we calculate the kinetic energy factor $W_k=1/2\int \boldsymbol{\xi}\cdot\boldsymbol{\rho}\cdot\boldsymbol{\xi}\, d^3r$ assuming $\boldsymbol{\rho}=\rho(\mathbf{I}-\boldsymbol{BB}/B^2)$ with $\rho=1$,[7,11] so that the kinetic energy becomes $W_k=1/2\int|\boldsymbol{\xi}_\perp|^2 d^3r$. In this case, the kinetic energy does not affect the stability (the sign of growth rate)

[a]Electronic mail: yamagisi@center.iae.kyoto-u.ac.jp

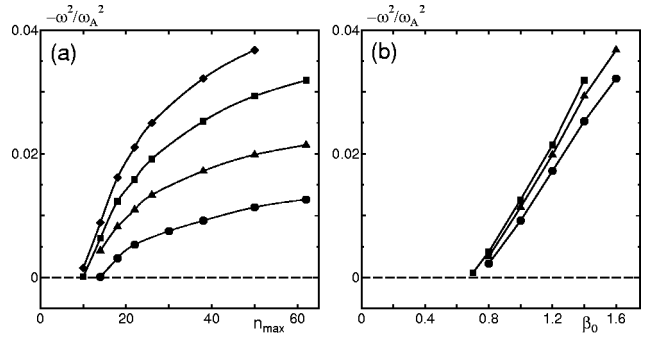

FIG. 1. (a) The most unstable eigenvalue as a function of maximum toroidal mode number $n_{\max}$, for the central beta, $\beta_0=1.0\%$ (circle); $\beta_0=1.2\%$ (triangle); $\beta_0=1.4\%$ (square); $\beta_0=1.6\%$ (diamond). (b) The most unstable eigenvalue as a function of beta, for the maximum toroidal mode number, $n_{\max}=38$ (circle); $n_{\max}=50$ (triangle); $n_{\max}=62$ (square). $N_F=2$ mode family is considered.

and is only used as the normalization. For the extremized plasma potential energy δW_p, the squared growth rate is then given as $\omega^2=\delta W_p/W_k$. This normalization is consistent with the standard local ballooning representation[12] assuming incompressibility, and we can compare the growth rates obtained for the local and global mode. Furthermore, the obtained growth rate is normalized by the Alfvén frequency $\omega_A^2=B_0^2/(\mu_0\rho R_0^2)$ such as $\lambda=\omega^2/\omega_A^2$, which we refer to as the eigenvalue. This procedure can compensate the different normalization of B in the equilibrium calculation.[13] Here, R_0 denotes the major radius at the center of helical coil and B_0 is the toroidally averaged magnetic field at $R=R_0$.

The perturbed modes are known to be classed with the mode families.[14] The mode families can be analyzed individually because of the absence of mode coupling among them. There are $1+[M/2]$ mode families labeled from 0 to $[M/2]$, and $N_f=0$ or $N_f=M/2$ mode families are comprised by the toroidal mode numbers, $n=|p|M+N_f$, whereas the other families are comprised by $n=pM+N_f$ or $n=pM-N_f$ with p being an integer. We first show the stability of $N_f=2(=M/2)$ mode family. Figure 1(a) shows $n_{\max}$ dependence of the most unstable eigenvalues, for several β_0 cases. Here, $\beta_0=2\mu_0 p(0)/B_0^2$ is a central beta value, and $n_{\max}$ is the maximum of the toroidal mode number used in the calculation. It can be seen that there is no low-n mode with $n<M$, and the lower limit of $n_{\max}$ exists for the instability. Figure 1(b) shows β_0 dependence of the most unstable eigenvalues, for some $n_{\max}$ cases. It can be seen that the beta limit is $\beta_0\sim 0.7\%$, which is slightly higher than the local $(n\to\infty)$ limit $\beta_0\sim 0.6\%$ previously estimated.[5] The eigenvalue is seen to be nearly linear on the beta. This dependence is distinct from that of the interchange mode. This is discussed in the following section. If the local analysis predicts the properties of global modes nicely, the higher n calculation will approach the local limit. The comparison between the local and the global modes is also shown in Sec. VI.

Figure 2 shows the modes corresponding to some eigenvalues shown in Fig. 1. The top frame shows the mode numbers used in the calculation. The second frame shows the radial profile of poloidal Fourier modes of the radial component of perturbation ξ^s_{mn}, with a fixed, most dominant toroidal mode number. The third frame shows the maximum value of each mode amplitude as a function of poloidal mode number, m. The numbers shown on the peaks in this figure denote the toroidal mode number. The bottom frame shows the contour of perturbation, ξ^s in the poloidal cross section $(\zeta=0)$. As is shown in the second frame, there are many poloidal modes for a fixed n, indicating strong poloidal mode coupling. On the other hand, it is seen in the third frame that there are modes having enough amplitude for numbers of n, which implies the strong toroidal mode coupling. As a result, the perturbation is clearly localized on the flux tubes, as shown in the bottom frame. This is the helical-type ballooning mode structure.

Since the difference of the stability properties between different mode families is not trivially predicted, we next show the comparison between the mode families. The $N_f=0$ or $N_f=M/2$ with even M mode family is comprised only by positive toroidal mode numbers. We thus expect property of these families not to differ too much. For the other mode families, on the other hand, there is the coupling between positive and negative number of toroidal modes. Since the mode in Heliotron J has strong toroidal mode coupling, as shown in Fig. 2, the stability may be different from that of mode families comprised by only positive n. In Fig. 3(a), the most unstable eigenvalue as a function of $n_{\max}(\lesssim 20)$ is shown, for $N_f=2(=M/2)$ and $N_f=1$ mode family. It can be seen that the spectra are reasonably on a curve, and the lower limit of $n_{\max}$ for the instability; $n_{\max}\sim 10$ still exists for both cases. Thus, insofar as there is the dependence of the most unstable eigenvalue on $n_{\max}$, the stability property of both families will be similar. Besides the most unstable eigenvalue, there may be several discrete unstable eigenstates. We denote n_q as a label of each eigenvalue ordered from the most unstable one, and call it eigen-number for convenience. In Fig. 3(b), the eigenvalues for $N_f=0$,1 and 2 mode families are shown as a function of eigen-number. Here, the $n_{\max}$ is taken to be nearly equal; $n_{\max}=36$, 37, and 38, correspondingly. It can be seen that the curves for the $N_f=0$ and $N_f=2$ mode families are similar, whereas the curve for the $N_f=1$ mode family is different from the others. Figure 4 clarifies the reason, where as in the third frame of Fig. 2, the mode belonging to the $N_f=1$ mode family with $n_{\max}=37$ is shown, for eigen-number $n_q=1$ [4(a)] and $n_q=2$ [4(b)]. From Fig. 4(a) it can be seen that the perturbation is comprised by almost positive toroidal mode numbers. This indicates that the positive number modes are hardly coupled with negative number modes. In this case, the eigenvalue will be insensitive to the distinction of mode family and will be dominated by $n_{\max}$ only, as shown in Fig. 3(a). The fact that the coupling is nonsignificant between the positive and negative n modes will allow another eigenstate where the negative n modes flourish. This is just the case of Fig. 4(b). The second $(n_q=2)$ eigenvalue is then nearly equal to the first $(n_q=1)$ eigenvalue, when the minimum of the toroidal mode number is nearly equal to the $-n_{\max}$. The situation may not be changed for the higher n_q so that the curve for the $N_f=1$ mode family shows steps, as shown in Fig. 3(b). These show that each eigenstate is basically similar for different mode families. Thus, it is valid in this study to investigate

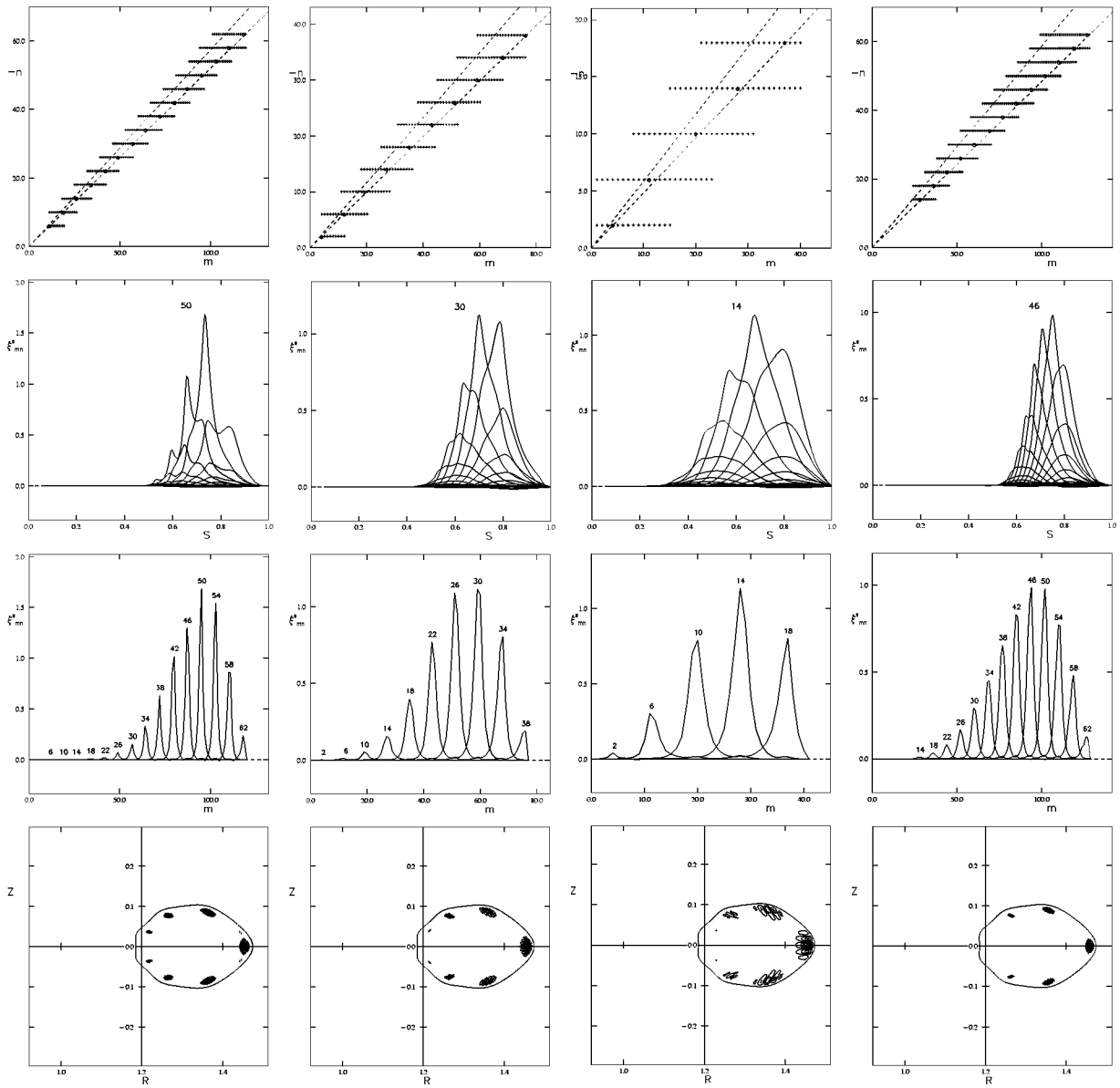

FIG. 2. (Top frame) Mode numbers used in the calculation. (Second frame) Radial profile of poloidal Fourier modes, ξ^s_{mn} with toroidal mode number for which mode has maximum amplitude. (Third frame) Measure of toroidal mode coupling (vide main). (Bottom frame) Contour of $\xi^s=\boldsymbol{\xi}\cdot\nabla s$ on a poloidal cross section ($\zeta=0$). Shown are cases for $[\beta_0(\%), n_{\max}, -\omega^2/\omega_A^2]=(0.8,62,4.146\times10^{-3})$; $(1.2,38,1.722\times10^{-2})$; $(1.4,18,1.237\times10^{-2})$; and $(1.4,62,3.187\times10^{-2})$; from left to right.

the $N_f=2$ mode family as a representation. This conserves the computational resources, compared with the case for the $N_f=1$ mode family with equivalent $n_{\max}$.

The excited modes in Heliotron J are of typically helical type, and these are destabilized independently of the Mercier criterion. The strong mode coupling, the lower limit of its toroidal mode number, the linear dependence of the eigenvalue curve on the beta, and the resulting mode structure are discussed in detail in the following sections.

III. RADIAL MODE STRUCTURE

For the interchange mode in the cylindrical plasma with only one toroidal and poloidal mode number, the properties of radial mode structure have been discussed.[15,16] Such an idealized mode does not oscillate along a field line, but does

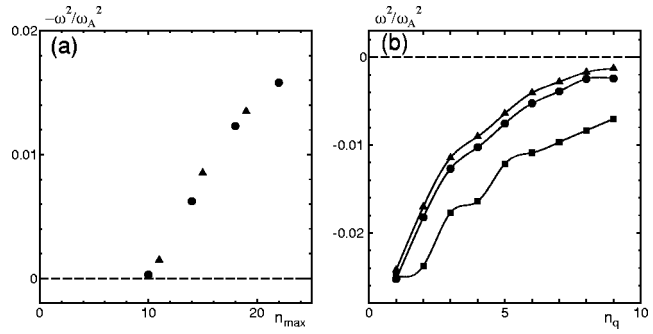

FIG. 3. (a) The most unstable eigenvalue at $\beta_0=1.4\%$ as a function of $n_{\max}(\lesssim 20)$, for $N_f=1$ (triangle) and $N_f=2$ (circle) mode families. (b) Unstable eigenvalue spectra at $\beta_0=1.4\%$ as a function of eigen-number n_q, for $N_f=0$ (triangle); $N_f=1$ (square); $N_f=2$ (circle). Maximum of toroidal mode number $n_{\max}$ is taken to be nearly equal; $n_{\max}=36, 37, 38$ for $N_f=0, 1, 2$ mode families, respectively.

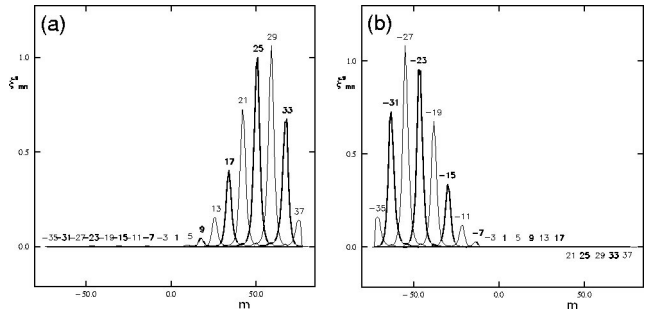

FIG. 4. Same plot as the third frame of Fig. 3 for the mode with $n_{\max}=37$ belonging to $N_f=1$ mode family at $\beta_0=1.4\%$, for (a) $n_q=1$ and (b) $n_q=2$ mode.

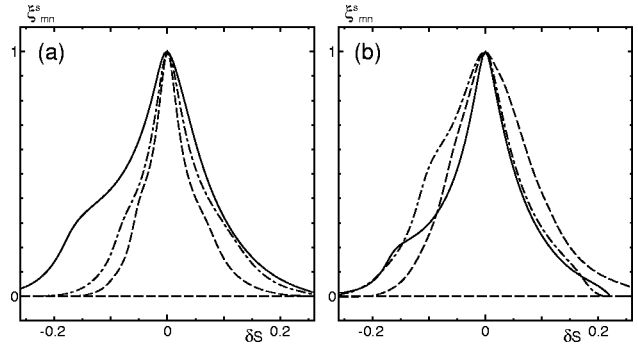

FIG. 5. Radial profile of maximum amplitude mode. (a) Maximum Fourier modes at $\beta_0=1.0\%$: $(m,n)=(27,14)$ (solid line); (58,30) (dash-dotted line); (97,50) (dashed line) which are for cases with $n_{\max}=18,38$, and 62, respectively. (b) Maximum Fourier modes with $n_{\max}=26$: $(m,n)=(42,22)$ (solid line); (44,22) (dash-dotted line); (37,18) (dashed line) which are for cases at $\beta_0=0.8\%$, 1.2%, and 1.6(%), respectively.

in the direction perpendicular to the field line with a constant wave number, on the corresponding rational surface. Away from the resonant surface, the mode needs energy to bend a field line, since the perturbation comes to deviate from the field line, which is the mechanism of the well-known shear-Alfvén stabilization. Since the higher n mode on the nonresonant surface has to bend the field line more rapidly, the shear-Alfvén stabilization should be more effective. Thus the higher n mode tends to localize more strongly around the resonant surface. It follows that the high-n interchange mode approximates to the Suydam mode, although the Suydam criterion can be derived without the assumption on the mode number.[17] This tendency was confirmed numerically in the cylindrical plasma by comparing the interchange stability and the Suydam criterion.[15] The other property of the interchange mode is that the mode is very localized on a rational surface when the beta is nearly marginal, whereas a mode tends to broaden its radial width at higher beta. This was also confirmed numerically in the above paper. This can be explained in that there exists residual free energy at higher than the marginal beta that overcomes the shear-Alfvén stabilization, and this allow a mode to broaden.[16]

The interchange mode in a realistic configuration also has the same properties, except that the effect of mode coupling exists.[8,13,18,19] The mode coupling is, however, not essential for the interchange stability. That is, if we purposely ignore the effect of coupling, the interchange mode is mostly destabilized as long as the Mercier criterion is violated. The existence of mode coupling will give rise to the possibility that the ballooning mode replaces the interchange mode as the most unstable one, as shown in Refs. 8 and 19. For this reason, the interchange mode obtained in the global calculation is usually $n \lesssim M$ mode. Even the low-n mode is strongly localized at the resonant surface near the critical beta, because there exists little residual energy. The mode then agrees well with the Mercier modes. Thus it follows that there is no limit of toroidal mode number for the instability in the Mercier unstable equilibrium. It is also noted that for the interchange mode the eigenvalue curve as a function of beta has nonlinear dependence as the beta decreases.[15,16] This is because the radial width of the interchange mode becomes extremely narrow, as the beta approaches the critical beta for the Mercier mode. This often causes the critical beta obtained by the global code using the finite difference to exceed the Mercier limit.[18]

In the Mercier stable equilibrium, as studied in this paper, the mode coupling is essential for the instability. The mode coupling to form the ballooning localization on a surface indicates that many modes have finite amplitude on the corresponding radial label, just as can be seen in Fig. 2. To see the radial mode structure in detail, the radial profile of the most dominant mode is shown in Fig. 5. Here, the origin is taken at the corresponding rational surface for each mode. Figure 5(a) shows the modes with the maximum amplitude in the cases for $n_{\max}=18$, 38, and 62 at a fixed beta, $\beta_0=1.0\%$. It can be seen that the radial width is narrower for the higher n mode. This is due to increasing shear-Alfvén stabilization, as noted above. Instead of this, the number of resonant surfaces increases with n, as can be seen in the top frame of Fig. 2. Thus, increasing n does not indicate weak mode coupling. Figure 5(b) shows for the maximum modes with $n_{\max}=26$ at $\beta_0=0.8\%$, 1.2%, and 1.6%. The mode width becomes broad near the rational surface at higher beta, as well as the interchange modes. Oppositely, the mode broadens out away from the rational surface at lower beta. This is not the case of the interchange mode, and indicates that the mode coupling is essential for the instability. When the beta decreases, the driving energy becomes low so that the amplitude of each mode goes down away from the corresponding resonant surface. Thus, as can be seen in the second frame of Fig. 2, the amplitudes of modes at a fixed radial position are smaller at the lower beta than the higher beta, which indicates that the mode coupling is weak. When the beta value decreases insomuch as the coupling cannot arise, these modes disappear suddenly, since the Mercier stability forbids such a mode to arise alone. Thus, the mode width is finite even near the marginal beta. This is the reason that the eigenvalue decreases linearly with decreasing beta, as shown in Fig. 1(b), which is in contrast to the case of the interchange mode as noted above.

We next discuss the radial oscillation of Fourier modes. Figure 6 shows the poloidal Fourier modes with $n=30$ for the $N_f=2$ mode family at $\beta_0=1.4\%$ and $n_{\max}=38$, for some label of eigenvalues (eigen-numbers) n_q. It can be seen that

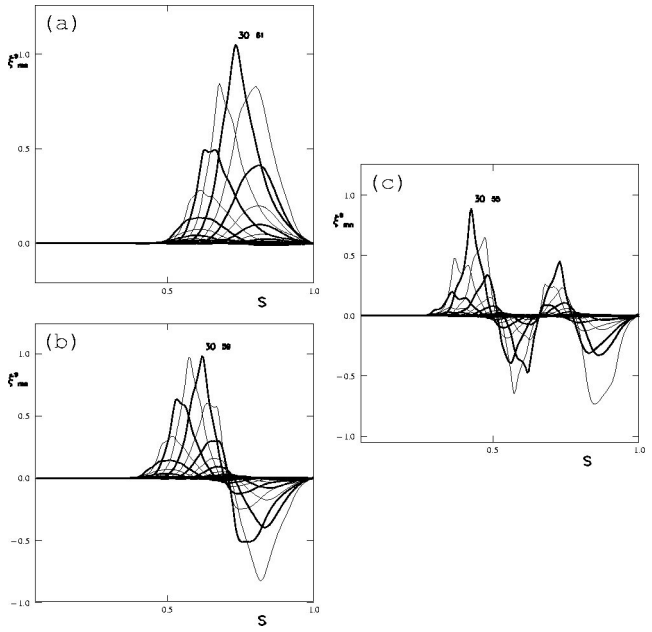

FIG. 6. Poloidal Fourier modes for $n=30$ ($\beta_0=1.4\%$, $n_{\max}=38$, $N_f=2$). Cases for $n_q=1,3,7$ are shown from left to right.

the number of radial nodes tends to increase with the n_q. According to the oscillation theorem (see, e.g., p. 304 of Ref. 17), the eigen number n_q is proportional to the radial node number, in a case where the mode coupling is ignorable. When the toroidal mode coupling is weak or ignorable, the toroidal mode number of perturbation, n will be specified uniquely. In this case the radial node number can be considered to be independent of the toroidal mode number. Actually, the toroidal mode number and the radial node number are separately taken into account in the quantization condition,[20] and are only applicable to the case of weak toroidal mode coupling (cylindrical isosurface of local eigenvalues). This tendency should be relaxed for the mode with strong mode coupling, since the eigen-number becomes a complicated function of the radial node number, poloidal-, and toroidal mode number. This is realized in Fig. 6 by seeing the difference between the radial node number and eigen-number with a fixed n. However, the most unstable mode still has zero node structure.

IV. MODE STRUCTURE ON A SURFACE

As is shown above, the perturbed mode in the Heliotron J plasma is strongly coupled toroidally as well as poloidally. This can be understood qualitatively from the magnetic field structure of Heliotron J. As is seen in Fig. 4 of Ref. 5, the normal curvature on a surface is strongly modulated in the toroidal direction. This means the strong nonaxisymmetry of the field, unlike the tokamak, and may explain why the modes with $n \gtrsim M$ in Heliotron J are not tokamak-like. The local analysis also shows the spherical isosurfaces of local eigenvalues in the (s,θ_k,α) space,[5] implying strong mode coupling. In this section we discuss the structure of helical-type ballooning mode on a rational surface.

As can be seen in Fig. 2 or Fig. 6, each Fourier mode (m_0,n_0) peaks at the resonant surface $q(s=s_0)=m_0/n_0$, with s being the radial label. The mode coupling occurs when the sideband modes are finite at the rational surface, $s=s_0$. One can see that such sets of sideband modes, $m_0 \pm 1, m_0 \pm 2, \ldots, m_0 \pm i$ meet at $s=s_0$. We can explain this by the shear-Alfvén dynamics, which restrains the bending of the field line. Considering a fixed toroidal mode number n_0, the poloidal sideband mode on a rational surface $q=m_0/n_0$ can be taken as $\xi_{m_0+i,n_0} \simeq \xi_{m_0-i,n_0} = \xi_{m_0,n_0[i]}$. Here it is assumed that a perturbation is Fourier decomposed as $\xi(s,\theta,\zeta)=\Sigma_{m,n}\xi_{m,n}(s)\cos(m\theta-n\zeta)$ for an even mode,[3] with θ and ζ being the poloidal and toroidal angle respectively, in the Boozer coordinates.[21] Then the perturbation on the surface $s=s_0$ can be written as

$$\begin{aligned}
&\xi_{m_0,n_0}(s_0,\theta,\zeta) \\
&\quad \simeq [\xi_{m_0,n_0[0]} + 2\{\xi_{m_0,n_0[1]}\cos\theta \\
&\qquad + \xi_{m_0,n_0[2]}\cos 2\theta + \cdots\}]\cos(m_0\theta - n_0\zeta) \\
&\quad = \left[\xi_{m_0,n_0[0]} + 2\sum_{i=1}^{M_c}\{\xi_{m_0,n_0[i]}\cos i\theta\}\right]\cos[n_0\alpha(s_0)], \quad (1)
\end{aligned}$$

where M_c is the number of sideband modes and normally $M_c \ll m_0$ for high-n modes, and $\cos(m+i)\theta+\cos(m-i)\theta = 2\cos m\theta\cos i\theta$ is used. Here, $\cos(m_0\theta-n_0\zeta)=\cos[n_0(\zeta - q(s_0)\theta)]=\cos[n_0\alpha(s_0)]$, and the argument of α is shown to make the radial dependence explicit. If we consider $\alpha=\zeta - q\theta$ and θ as independent variables instead of Boozer angles θ and ζ, then θ can be considered as a variable along a field line, and α as a variable perpendicular to a field line (see, e.g., Ref. 12). Equation (1) shows that a mode on the rational surface can be localized along a field line by the poloidal mode coupling, whereas the rapid oscillation due to the high n_0 is only in the perpendicular direction. The shear-Alfvén stabilization does not take affect in this direction, so that this will explain how the high-n tokamak (and tokamak-like) ballooning modes can be excited against the stabilization. It is important to note that the poloidal mode coupling occurs through the difference from the m_0 and is independent of the value of m_0 itself. Thus, the high-$n(m)$ mode number is not essential to form the tokamak-like ballooning structure. In principle, relatively low-n tokamak-like ballooning can be excited as long as there are many sideband modes.

For the high-$n,n \gg M$ modes in the helical systems, we can see toroidal mode coupling by summing up Eq. (1) for different toroidal mode number modes. On the $q(s')=m'/n'$ rational surface near the rational surface $q(s_0)=m_0/n_0$, a mode is written as Eq. (1) for the mode number (m',n'). Now, the rapid phase originating from the rational surface $q(s')=m'/n'$ is expressed by $n'\alpha(s')=n'[\zeta - q(s')\theta]$. The shear-Alfvén dynamics will require that this is approximately in phase on the surface $q(s_0)=m_0/n_0$. When the distance between the rational surfaces is short, such that the shear $q'=dq/ds$ can be considered as a constant, we can write $q(s')=q(s_0)+q'(s_0)\Delta s'$. Here, $\Delta s'$ is the distance between m'/n' and m_0/n_0 rational surfaces, and so $\Delta s'=|m'/n'-m_0/n_0|/q'(s_0)$. Denoting Δs as the dis-

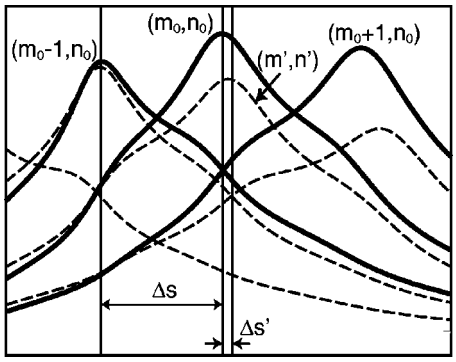

FIG. 7. Schematic of coupled modes. Main mode (m_0,n_0) is poloidally coupled (solid) and toroidally coupled (dashed) with sideband modes. (This is the $q'>0$ case.)

tance between the rational surfaces with the fixed toroidal mode number n_0, $\Delta s'$ can be shorter by a factor of $1/n'$ than Δs, since the minimum distance for two fractions with the same denominator n_0 is $1/n_0$, while that for the denominators n_0 and n' is $1/(n_0 n')$. The situation is illustrated in Fig. 7. Then, the poloidal mode number m' will satisfy $|m'/n' - m_0/n_0| \simeq 1/(n_0 n')$. The rapid phase from the (m',n') mode on the m_0/n_0 surface then becomes $n'\alpha(s') \simeq n'\alpha(s_0) - \theta/n_0 \simeq n'\alpha(s_0)$. It follows from the discussion of the mode family[14] that the sets of such sideband modes, $(m',n')=(m_j,n_j)$, will satisfy

$$n_j = n_0 + jM, \quad |m_j n_0 - m_0 n_j| \simeq 1 \ll n_0, \tag{2}$$

where $j \ll N_c$ is an integer with $N_c (\ll n_0)$ being the number of toroidal sideband modes. The amplitude of the (m',n') mode on $s=s_0$ will be nearly equivalent on $s=s'$, so that the mode on $s=s_0$ can be written as

$$\xi_{m_0,n_0}(s_0,\theta,\alpha) \simeq \sum_{j=-N_c}^{N_c} [A_j(\theta)\cos(n_j \alpha(s_0))], \tag{3}$$

where

$$A_j(\theta) = \xi_{m_0,n_0[0,j]} + 2\sum_{i=1}^{M_{c[j]}} [\xi_{m_0,n_0[i,j]} \cos i\theta].$$

Here, $\xi_{m_0,n_0[i,j]}$ is the amplitude for the $(m_j \pm i, n_j)$ mode satisfying Eq. (2), and $M_{c[j]}$ is considered as the number of poloidal sideband modes for m_j mode. To simply see the implication, we consider only one toroidal sideband mode n_j, and assume that A_j is equal for different j. In this case, the mode on the rational surface $s=s_0$ becomes

$$\xi_{m_0,n_0}(s_0,\theta,\alpha) \simeq 2\cos[(jM/2)\alpha(s_0)] A_j(\theta)\cos[n_0\alpha(s_0)], \tag{4}$$

where $(n_0+n_j)/2 = (2n_0+jM)/2 \simeq n_0$ and $(n_j-n_0)/2 = jM/2$ are used. Again the rapid oscillation is only in the perpendicular direction, because of the assumption $M \ll n_0$. This takes the form of the well-known undulation in the α direction arising from superimposing waves nearly in phase. That is, the mode can be localized along the field line as usual ballooning, while wave packets are formed in the perpendicular direction as a result of the slow variation of amplitude. This causes the mode to localize on the flux tube,

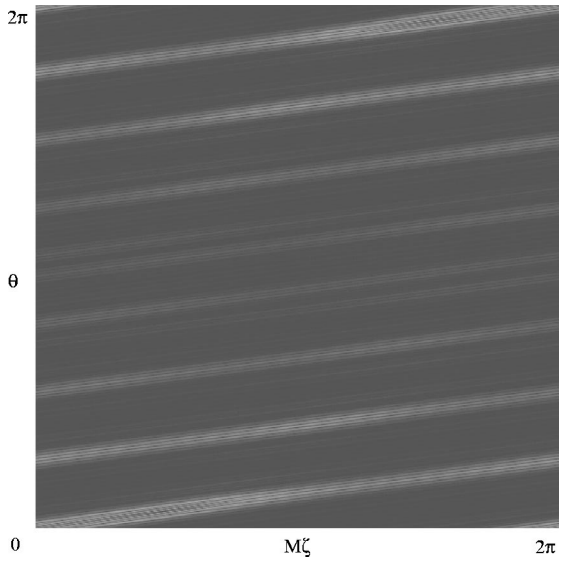

FIG. 8. Contour of perturbation $\xi^s = \boldsymbol{\xi}\cdot\nabla s$ in $\theta - M\zeta$ plane ($n_{\max}=62$, $\beta_0 = 1.0\%$, $s=0.7$).

and the helical type ballooning structure is formed. In Fig. 8, a typical mode structure in the Heliotron J plasma is shown. It is clear that a mode cannot be expressed as Eq. (4) if M/n is not so small. In other words, in the helical systems, the toroidal mode coupling obstructs the low-n ballooning modes to be unstable through the imperative shear-Alfvén stabilization. This will explain the reason for the lower limit of toroidal mode number for the instability, as shown in Fig. 1(a).

V. CONTRIBUTIONS TO THE ENERGY

We investigate the contributions from the equilibrium quantities to the potential energy in this section. The expression for the potential energy in terms of the perturbed functions used in the CAS3D code is given in Ref. 3. In considering the correspondence to the local ballooning formalism, another useful expression is that of Greene and Johnson[22]

$$W_p = \frac{1}{2}\int\int\int ds\, d\theta\, d\zeta \sqrt{g}\ [|\boldsymbol{Q}_\perp|^2 + |C^3|^2 + A_p + A_c], \tag{5}$$

where

$$\sqrt{g}|\boldsymbol{Q}_\perp|^2 = \frac{1}{\sqrt{g}|\nabla s|^2}|\sqrt{g}\boldsymbol{B}\cdot\nabla\xi^s|^2 + \frac{|\nabla s|^2}{\sqrt{g}B^2}|\sqrt{g}\boldsymbol{B}\cdot\nabla(\eta + \mathcal{R}\xi^s) - \sqrt{g}S_*\xi^s|^2, \tag{6}$$

$$\sqrt{g}A_p = -2\mu_0(\boldsymbol{\xi}_\perp\cdot\nabla p)(\boldsymbol{\xi}_\perp\cdot\boldsymbol{\kappa})\sqrt{g} = -\frac{2\mu_0 p'\sqrt{g}\kappa^s}{|\nabla s|^2}|\xi^s|^2 - \xi^s(\eta + \mathcal{R}\xi^s)\sqrt{g}\boldsymbol{B}\cdot\nabla\sigma = A_{pn} + A_{pg}, \tag{7}$$

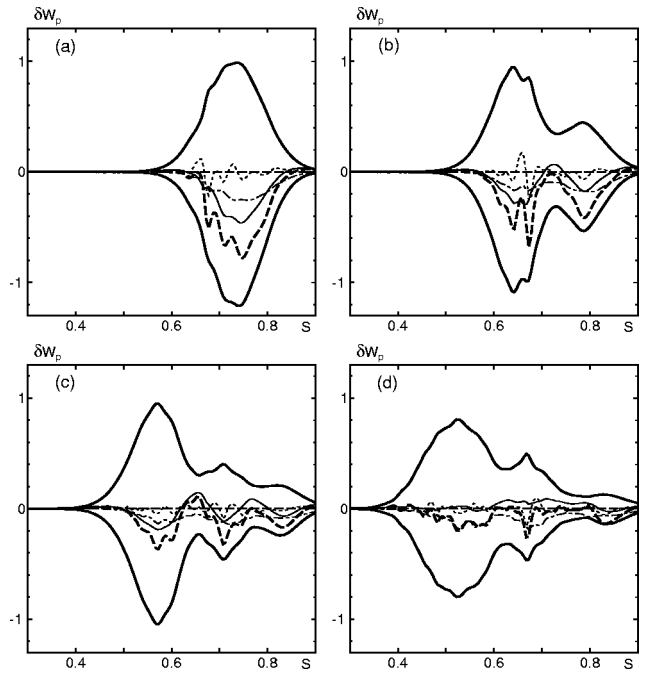

FIG. 9. Perturbed potential energies for modes with $n_{\max}=62$ at $\beta_0=1.4\%$. The two thick solid lines are shear-Alfvén stabilization, $\langle|\boldsymbol{Q}_\perp|^2\rangle$ (upper) and normal curvature term, $\langle A_{pn}\rangle$ (lower), which are scaled by a factor of 0.5. The thin solid line is the sum of these, $\langle|\boldsymbol{Q}_\perp|^2\rangle+\langle A_{pn}\rangle$. The thin dashed and dash-dotted lines correspond to the current-driven term $\langle A_c\rangle$ and geodesic curvature term $\langle A_{pg}\rangle$, respectively. The thick dashed line represents the potential energy δW_p. Here $\langle\cdot\rangle=\int\cdot\sqrt{g}d\theta\,d\zeta$. (a)–(d) correspond to the number of eigenvalue (eigen-number) $n_q=1$, 4, 9, and 16, respectively.

$$\sqrt{g}A_c=-\sigma(\boldsymbol{\xi}_\perp\times\boldsymbol{B})\cdot\boldsymbol{Q}_\perp\sqrt{g}$$
$$=\sigma[\xi^s\sqrt{g}\boldsymbol{B}\cdot\nabla\eta-\eta\sqrt{g}\boldsymbol{B}\cdot\nabla\xi^s]-\sigma\sqrt{g\overline{S}_*}|\xi^s|^2. \quad (8)$$

Here, s is the normalized toroidal flux, and θ and ζ the poloidal and toroidal angle, respectively in Boozer coordinate.[21] $\xi^s=\boldsymbol{\xi}\cdot\nabla s$ and $\eta=(\boldsymbol{\xi}\times\boldsymbol{B})\cdot\sqrt{g}\nabla\theta\times\nabla\zeta$ are perturbed functions used in CAS3D2. $\sigma=\mu_0\,\boldsymbol{j}\cdot\boldsymbol{B}/B^2$ denotes the local (Pfirsch–Schlüter) current, and the effect of curvature is included as $\kappa^s=\boldsymbol{\kappa}\cdot\nabla s$ and $\kappa_g=\boldsymbol{\kappa}\cdot\boldsymbol{B}\times\nabla s=(\boldsymbol{B}\cdot\nabla\sigma)B^2/2\mu_0p'$, the normal and the geodesic curvature, respectively. The local shear S_* is given as

$$S_*=\frac{\boldsymbol{B}\times\nabla s}{|\nabla s|^2}\cdot\nabla\times\frac{\boldsymbol{B}\times\nabla s}{|\nabla s|^2}=\frac{1}{\sqrt{g}}\psi'^2\iota'+\boldsymbol{B}\cdot\nabla\mathcal{R}=\overline{S}_*+\widetilde{S}_*, \quad (9)$$

where $\overline{S}_*$ and $\widetilde{S}_*$ are the global shear and the residual shear, respectively, and $\mathcal{R}=(\chi'\nabla\zeta-\psi'\nabla\theta)\cdot\nabla s/|\nabla s|^2$ is the integrated residual shear.[20] Here $2\pi\chi(2\pi\psi)$ is the poloidal(toroidal) flux, and the prime denotes the derivative with respect to s. The stabilization due to the magnetic compression, $C^3=(\boldsymbol{Q}\cdot\boldsymbol{B}-\mu_0\boldsymbol{\xi}\cdot\nabla p)/B=-B(\nabla\cdot\boldsymbol{\xi}_\perp+2\boldsymbol{\xi}_\perp\cdot\boldsymbol{\kappa})$ have little contribution to the energy for the shear-Alfvén modes ($k_\perp\gg k_\parallel$),[11,12] and this is actually the case in the numerical calculation.[3] We will omit this term below. $|\boldsymbol{Q}_\perp|^2$ represents the shear-Alfvén stabilization, and $A_p=A_{pn}+A_{pg}$ is the sum of the normal and geodesic curvature-driven energy. A_c represents the current-driven energy.

Figure 9 shows the radial profile of the potential energy above for the modes corresponding to several n_q, the label of unstable eigenvalues ordered from the most unstable one. For the more unstable, small n_q modes, the normal curvature term A_{pn} overcomes the shear-Alfvén stabilization, and the potential energy becomes negative, thus indicating the instabilities. The current-driven term A_c is oscillating and takes only a small contribution aboard. This contribution affects the mode but does not destabilize the mode itself, since the oscillating energy vanishes by the integration in the whole plasma. As the n_q increases, the cancellation between $|\boldsymbol{Q}_\perp|^2$ and A_{pn} becomes exact. Then, the geodesic curvature and the current-driven term become important. The energy profile for these modes extends radially, while that for the most unstable ballooning modes localizes around the region of large pressure gradient. In the standard ballooning formalism,[12] the current-driven term is dropped for ordering and the geodesic curvature plays only a subordinate role in the stability of localized modes. Hence it may be difficult to treat the higher n_q modes in the local stability correctly.

We now concentrate on the most unstable mode, and the role of equilibrium quantities is discussed. From above, it is valid to eliminate the current-driven term. A useful property was found that η_{mn} tends to vanish at the peak of ξ^s_{mn}, i.e., the corresponding rational surface.[4] Ignoring η in Eqs. (6) and (7) as a result, the perturbed functions involved are in the quadratic form, except for the second term in $|\boldsymbol{Q}_\perp|^2$. We can further reduce this term by Eq. (9) as $|\mathcal{R}\sqrt{g}\boldsymbol{B}\cdot\nabla\xi^s-\sqrt{g\overline{S}_*}\xi^s|^2|\nabla s|^2/(\sqrt{g}B^2)$. Thus, the integrated local shear and the global shear is essential, as well as the local ballooning formalism. However, the integrated local shear does not differ from the local shear as much as that we discussed with the local shear. In this case, the equilibrium functions can be separated from the perturbed functions, and the important functions for the stability turn out to be: the local shear S_* in $|\boldsymbol{Q}_\perp|^2$, and the destabilizations due to the curvature, $-2\mu_0p'\sqrt{g}\kappa^s/|\nabla s|^2$ and $-\mathcal{R}\sqrt{g}\boldsymbol{B}\cdot\nabla\sigma$. In Fig. 10, these quantities are shown on a surface. In this figure, red (blue) color indicates positive (negative) value, and the negative region contributes to the instability. It is seen from (c) that the negative normal curvature excites the perturbation. As shown in (d), the term relating to the product of the geodesic curvature and the integrated residual shear $\mathcal{R}$ have similar profile to the normal curvature, although the $\sqrt{g}\boldsymbol{B}\cdot\nabla\sigma$ and $\mathcal{R}$ itself have an odd distribution on the stellarator symmetric point. Then, it destabilizes the mode as well, as is also seen in Fig. 9. The same conclusion has also been pointed out in the local analysis of the kinetic mode.[23] As for the local shear shown in (b), the perturbation seems to be excited in the positive shear region. However, this term is squared in the stabilizing $|\boldsymbol{Q}_\perp|^2$, so it may be misleading. As seen in Eq. (9), the local shear is inversely proportional to the term $|\nabla s|^2$, which is a measure of surface interval and so is related closely to the Shafranov shift. Thus, the local shear decreases the magnitude in the outboard of the plasma. Thus in Fig. 9 it should be seen that the perturbation passes through the margin of positive local shear region, to avoid the stabilization. This is consistent with the role of ''integrated'' local

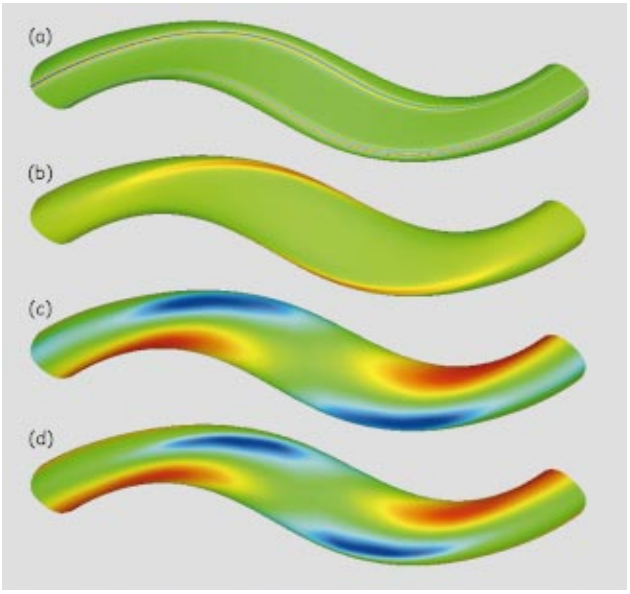

FIG. 10. (Color) Perturbed and equilibrium functions on one field period viewed from the outboard side, at $\beta_0=1.4\%$, $s=0.7$. (a) Perturbation ξ^s with $n_{\max}=38$; (b) local shear S_*; (c) normal curvature $-2\mu_0 p'\boldsymbol{\kappa}\cdot\nabla s\sqrt{g}/|\nabla s|^2$, and (d) geodesic curvature $-\mathcal{R}\sqrt{g}\boldsymbol{B}\cdot\nabla\sigma$.

shear on the local stability,[24] where disappearance of it deteriorates the stability.

VI. COMPARISON BETWEEN GLOBAL AND LOCAL MODES

It is interesting to see how the local modes relate to the global modes. This is the purpose of this section. In Fig. 11, the local and global eigenvalues are shown as a function of $1/n_{\max}$, for several betas. The local eigenvalues are obtained by the ballooning equation, taking the radially maximum value with $(\theta_k,\alpha)=(0,0)$, and are shown at $1/n_{\max}=0$. The choice of $\theta_k=0$ is valid for the comparison with the most unstable (zero node) mode, since θ_k represents a radial wave number.[12] It can be seen that the decrease of $1/n_{\max}$ makes

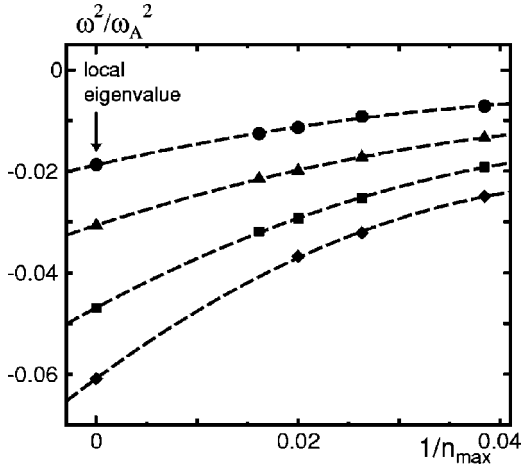

FIG. 11. Global and local eigenvalues at $\beta_0=1.0\%$ (circle); 1.2% (triangle); 1.4% (square); 1.6% (diamond). Local eigenvalues shown at $1/n_{\max}=0$ are radially maximum value with $(\alpha,\theta_k)=(0,0)$.

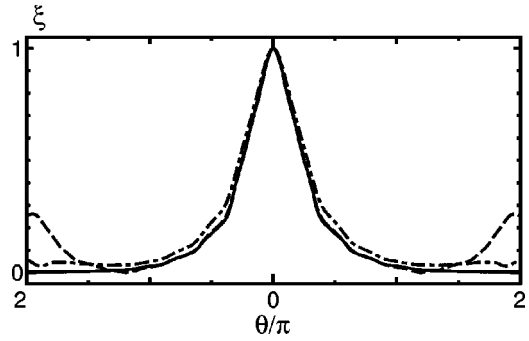

FIG. 12. Mode structure along a field line at $\beta_0=1.6\%$ and $s=0.7$. Local mode with $(\theta_k=0,\alpha=0)$ is shown by solid line. Global modes ($|\xi^s|$) for $n_{\max}=62$ and $n_{\max}=22$ are shown by dashed and dash-dotted lines, respectively. The global mode approximates to the local mode with increasing n.

the global eigenvalues approach the local one monotonically. This indicates that the global modes for the higher n calculation approaches the local one by degrees. The corresponding mode structure along a field line is shown in Fig. 12. The local mode recovers well the global mode, although it does not have the periodicity. It can be seen that the global mode with higher n is more approximate to the local mode.

From the comparison of modes obtained locally and globally, it is expected that the degree of the poloidal mode coupling is well calculated from the local modes. To see this, we show the Fourier decomposition of the local mode along the field line over $-\pi\leqslant\theta\leqslant\pi$ by the dashed lines, in Fig. 13. Here, the radial label for the local mode is taken to correspond to the location of the maximum amplitude of global modes shown for comparison ($s=0.7$). The degrees of the mode coupling of the global mode are determined by the intersections between the main and the sideband modes, which are shown by circle points at the reference surface. It is shown that the degrees of poloidal mode coupling are recovered well from the local mode, although the global modes have many other modes due to the toroidal coupling. This guarantees the result in Sec. IV that the mode structure along a field line, i.e., $A_j(\theta)$, is practically determined by the poloidal mode coupling.

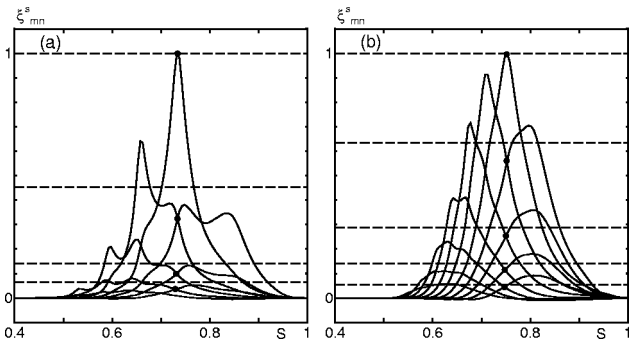

FIG. 13. Global Fourier modes with $n_{\max}=62$ are shown with a fixed n for the maximum amplitude, and Fourier decomposition of local mode with $(\alpha,\theta_k)=(0,0)$ along a field line is shown by dashed lines, at (a) $\beta_0=0.8\%$ and (b) $\beta_0=1.4\%$. The local mode is Fourier decomposed over $[-\pi,\pi]$ along the field line on the surface that corresponds to the location of the maximum of global amplitude. The circle points denote the intersections between the main and the sideband modes at the reference surface.

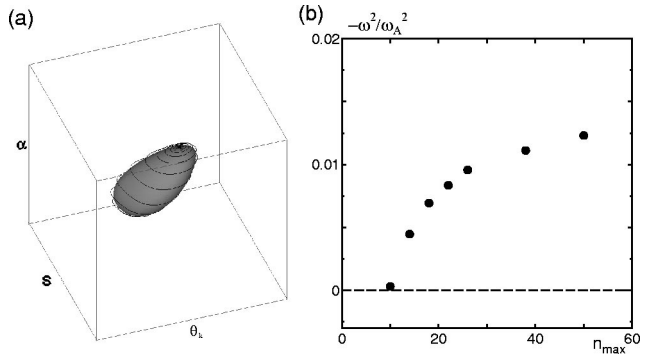

FIG. 14. (a) Isosurface of local eigenvalue in (s,θ_k,α) space $(0\leqslant s\leqslant 1, -\pi\leqslant\theta_k, M\alpha\leqslant\pi, \omega^2/\omega_A^2=-1.518\times10^{-2})$. A ray trajectory wraps around the surface. (b) Global eigenvalues for $N_f=2$ mode family as a function of $n_{\max}$ (peaked pressure profile, $\beta_0=1.6\%$).

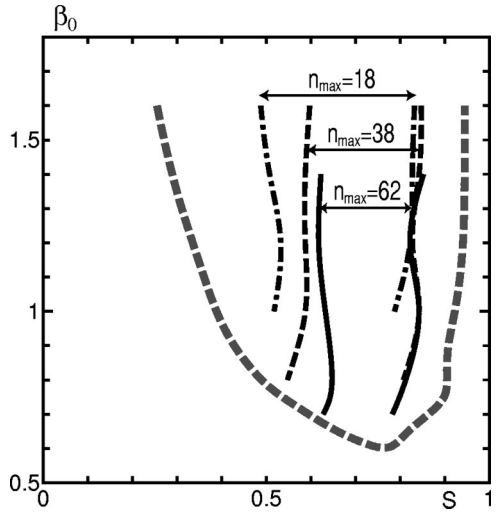

FIG. 15. Unstable region on $s-\beta_0$ plane. Negative region of global mode energy δW_p is shown for $n_{\max}=18$ (dash-dotted lines); 38 (dashed lines); and 62 (solid lines) cases. Unstable region for local modes with $(\theta_k,\alpha)=(0,0)$ is shown by thick dashed line.

Recently a formula for estimating the global toroidal mode number from the local eigenvalues has been proposed.[25] Following this, the lower limit of the toroidal mode number for the instability is given as

$$n_{\text{limit}}\sim(8\pi^2/v_{3D})^{1/2}. \tag{10}$$

Here, v_{3D} is a volume in the (s,θ_k,α) space for a spherical isosurface with specific local eigenvalue. To determine the lower limit, a nearly marginal, local eigenvalue should be specified for which the volume of isosurface is the largest. However, the local ballooning formalism cannot apply in the shearless regime,[12] which leads to a distorted isosurface. For a case of the broad pressure profile, it is difficult to estimate the volume of isosurface, since the weak shear range wraps over the large pressure gradient range and so affects the local eigenvalue remarkably. We thus consider a case of a peaked pressure profile; $p=p(0)(1-\hat{\chi})^2$ with $\hat{\chi}$ being a normalized poloidal flux $(\beta=1.6\%)$. Then, the isosurface should be specified as large as possible, for which a ray trajectory[12] can be followed, as shown in Fig. 14(a). The global eigenvalues of $N_f=2$ family are shown in Fig. 14(b) for comparison. The volume of isosurface in this case can be calculated as being about $v_{3D}\sim0.27$, so that the lower limit of the toroidal mode number is $n_{\text{limit}}\sim17$. This seems to be reasonable in comparing with the global limit, which is about 10. However, the quantitative estimate will require the global analysis.

In Fig. 15, negative range of the potential energy of the global mode is compared with the unstable range for the local mode with $(\theta_k,\alpha)=(0,0)$, in the $s-\beta_0$ plane. The lines for different $n_{\max}$ are cut below at different beta and this indicates that the critical beta is different. It can be seen that the negative energy range is broad even where the beta is nearly critical. It follows that the radial width of modes is finite even at the critical beta, as discussed in Sec. III. Then as $n_{\max}$ increases, the critical beta of the global mode can be approximated to that of the local mode well enough. This is in contrast to the case of the interchange mode. In that case there exists a gap between the local (Mercier) beta limit and global (interchange) limit, which is the so-called soft beta limit, since the radial width of global mode becomes extremely narrow near the marginal beta.[18] It is also seen that the higher n global mode has a narrower width, and vice versa. This indicates that the global mode is very localized radially in the high-n limit, and the width approaches the unstable range of the local modes at the critical beta. Oppositely, it is supposable that the wide unstable range of the local mode indicates the existence of the lower n mode. This indicates that even though the local mode cannot be stabilized fully, the narrow unstable range in the radial direction is still significant to stabilize the finite n modes. This will encourage the optimization study against the ballooning modes.

VII. CONCLUSIONS

We investigated the stability of the global ideal ballooning mode in the standard Heliotron J plasma, and discussed the properties of destabilized modes. It is shown that the modes are typically helical type, as expected from the local analysis. Such modes are destabilized independently of the Mercier modes, and the interchange mode is not found. We noted that the helical ballooning mode is not low-n to avoid the shear-Alfvén stabilization, which may be different from the tokamak-type ballooning mode. Actually, the dominant mode is not low-n, so that the mode is not the global type in the Heliotron J plasma. Thus, the kinetic effect will be important. As was also shown in Sec. IV, the distance between the rational surfaces is inversely proportional to q' as well as n. Thus, the increasing shear makes the shear-Alfvén stabilization stronger, while it narrows the distance between the rational surfaces. This indicates that the sideband modes can reach to the other mode rational surface as it suffers stabilization over the short range. Hence, the increasing shear is two-faced for the mode coupling. Similarly, as the shear decreases, the sideband modes suffer the shear-Alfvén stabilization over a long range, to couple with the other mode, but the stabilization itself becomes weak. The weak mode coupling indicates that the mode can spread over the surface. Thus, when the configuration is in the magnetic well with very weak shear, there is a possibility that the mode enters

the stable regime. This indicates the same role of the global shear on the first and second stability regime in the $\bar{s}-\bar{\alpha}$ diagram in the local analysis,[26] where $\bar{s}$ and $\bar{\alpha}$ mean the shear and the pressure gradient, respectively. It should be noted that the localization on the surface has two degrees of freedom in the helical system. The localization indicates the rapid growth of the perturbation. This may explain the result of Refs. 8 and 19 that the most unstable mode is usually the ballooning type even in the Mercier unstable equilibrium, as the number of the sideband modes increase. The comparison between the local and global modes showed good agreement, on the eigenvalues as well as the mode structure. The global kinetic modes are actually hard to study, but it is expected that the local analysis such as in Ref. 27 can predict the global results in the helical system well enough.

In this study we show the stability results only in the standard Heliotron J plasma. From the results in this paper, we can propose the scenario of stabilizing the ballooning modes as follows. Sufficiently high-n mode will be stabilized by the kinetic effect, whereas sufficiently low-n mode is stable owing to the good Mercier stability. Hence, it is important to prevent the moderate-n mode from being destabilized. Such a mode will be relatively extended along a field line and so may be near the second stability regime in the $\bar{s}-\bar{\alpha}$ space, together with the deep magnetic well. We supposed in Sec. VI that the lower limit of the destabilized toroidal mode number becomes high when the locally unstable range in the radial direction becomes narrow. Thus, what we should do to attain the second stability is decrease the global shear in order to make the destabilized toroidal mode number high. The optimization study will be our future work.

ACKNOWLEDGMENTS

The authors thank Dr. C. Nührenberg for use of the CAS3D code. The calculations in this work have been carried out on the NEC-SX5 supercomputer at the National Institute for Fusion Science.

APPENDIX: MODE SELECTION

Mode numbers of a perturbation are given as an input for the CAS3D stability code. For the analysis of the high-n mode proposed in this study, it is hard for the computation to consider all the modes below a maximum toroidal mode specified. Thus, we need to select perturbed modes properly. Each mode is typically destabilized by the energy rising from a corresponding rational surface. However, such a mode will need to couple with another mode which may be off-resonant. Hence, it is incorrect to consider only resonant modes. As is well known, the ballooning mode is susceptible to the normal curvature, of which the (Boozer) Fourier harmonics is similar to the magnetic field spectra. In the Heliotron J equilibrium in this study, the dominant B spectra are $(m_e,n_e)=(1,4),(0,4),(1,0)$, the helical, bumpy, and toroidal components, respectively.[1] Then, we should consider the helical and bumpy coupling $(n_e\neq 0)$ for fear of ignoring the effect of the toroidal mode coupling on the stability. This procedure is shown in Fig. 16. In this figure, $N_f=1$ mode family is considered, with the maximum and minimum of toroidal mode number, $n_{\max}=19$ and $n_{\min}=-17$. As is shown in Fig. 16(a), in which the resonant modes only are considered, there is a possibility that a mode with mode number (m,n) likely does not have a coupling pair with the mode number $(m,n)\pm(1,4)$ or $(m,n)\pm(0,4)$. So, we add the off-resonant modes, as shown in Fig. 16(b). In this case, any resonant modes can have a helical or bumpy coupling pair. This also assisted with the coupling poloidally with the off-resonant modes for any fixed n modes.

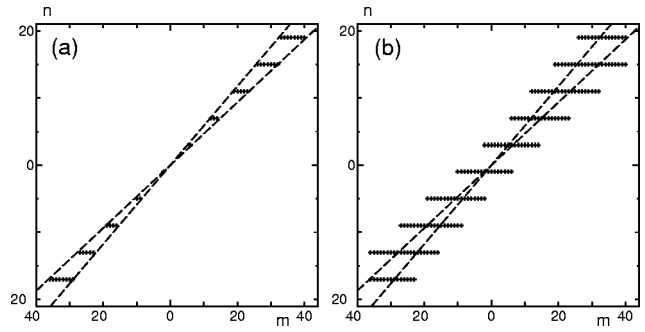

FIG. 16. Method of mode selection in an example of $N_f=1$ mode family. (a) Case for resonant modes only. Modes with resonant surfaces $\epsilon=n/m$ are given as contained by two dashed lines, which correspond to the maximum and the minimum of rotational transform $\times m$. (b) Case of considering off-resonant modes as well as resonant modes. In this case, helical or bumpy coupling, $\pm(1,4),\pm(0,4)$ can occur for any resonant modes, except for the edge of toroidal spectra.

It is noted that when n becomes sufficiently high, the important region for stability moves far from the origin in the Fourier space, because the high-n mode is usually more unstable than the low-n mode. In this study, we thus often neglect small number modes in the high-n calculation, since the effect of doing so is small for the stability, but large for the computational memory and time.

[1] M. Wakatani, Y. Nakamura, K. Kondo *et al.*, Nucl. Fusion **40**, 569 (2000).
[2] T. Obiki, T. Mizuuchi, K. Nagasaki *et al.*, Nucl. Fusion **41**, 833 (2001).
[3] C. Schwab, Phys. Fluids B **5**, 3195 (1993).
[4] C. Nuhrenberg, Phys. Plasmas **6**, 137 (1999).
[5] O. Yamagishi, Y. Nakamura, and K. Kondo, Phys. Plasmas **8**, 2750 (2001).
[6] N. Nakajima, Phys. Plasmas **3**, 4556 (1996).
[7] P. Cuthbert, J. L. Lewandowski, H. J. Gardner, M. Persson, D. B. Singleton, R. L. Dewar, N. Nakajima, and W. A. Cooper, Phys. Plasmas **5**, 2921 (1998).
[8] J. Chen, N. Nakajima, and M. Okamoto, Phys. Plasmas **6**, 1562 (1999).
[9] N. Nakajima, *Fusion Energy 2000, Proceedings of the 18th IAEA Fusion Energy Conference, Sorrento*, 2000 (IAEA, Vienna, to be published).
[10] S. P. Hirshman, Phys. Fluids **26**, 3553 (1983).
[11] R. L. Dewar, J. Plasma Fusion Res. **73**, 1123 (1997).
[12] R. L. Dewar and A. H. Glasser, Phys. Fluids **26**, 3038 (1983).
[13] Y. Nakamura, T. Matsumoto, M. Wakatani *et al.*, J. Comput. Phys. **128**, 43 (1996).
[14] W. A. Cooper and G. Y. Fu, in *Theory of Fusion Plasmas Varenna 1990* (Editrice Compositori, Bologna, 1990), p. 655.
[15] H. Sugama and M. Wakatani, J. Phys. Soc. Jpn. **58**, 1128 (1989).
[16] T. Tatsuno, M. Wakatani, and K. Ichiguchi, Nucl. Fusion **39**, 1391 (1999).
[17] J. P. Freidberg, *Ideal Magnetohydrodynamics* (Plenum, New York and London, 1987).
[18] Y. Nakamura, K. Ichiguchi, M. Wakatani, and J. L. Johnson, J. Phys. Soc. Jpn. **58**, 3157 (1989).
[19] G. Y. Fu, W. A. Cooper, R. Gruber, U. Schwenn, and D. V. Anderson, Phys. Fluids B **4**, 1401 (1992).

[20]R. L. Dewar and D. A. Monticello, Phys. Fluids **27**, 1723 (1984).
[21]W. D. D'haeseleer, W. N. G. Hitchon, J. D. Callen, and J. L. Shohet, *Flux Coordinates and Magnetic Field Structure* (Springer-Verlag, Berlin, Heidelberg, 1991).
[22]J. M. Greene and J. L. Johnson, Plasma Phys. **10**, 729 (1968).
[23]J. L. V. Lewandowski, Plasma Phys. Controlled Fusion **40**, 283 (1998).
[24]N. Nakajima, Phys. Plasmas **3**, 4545 (1996).
[25]R. L. Dewar, P. Cuthbert, and R. Ball, Phys. Lett **86**, 2321 (2001).
[26]J. M. Greene and M. S. Chance, Nucl. Fusion **21**, 453 (1981).
[27]G. Rewoldt, L.-P. Ku, and W. M. Tang, Phys. Plasmas **6**, 4705 (1999).